communications engineering

A Nature Portfolio journal

Article

https://doi.org/10.1038/s44172-025-00395-5

Addressing optical modulator non-linearities for photonic neural networks

Peter Seigo Kincaid [1], Nicola Andriolli [2], Giampiero Contestabile [1] & Lorenzo De Marinis [1]

Within the context of neuromorphic computing, analog photonics, especially after the advent of photonic integrated technologies, offers unparalleled computing speeds per core, and the reduction of size and power consumption compared to digital electronics. However, the functionality of analog systems is limited by noise and non-linear distortions, which degrade signal resolution. Here, a method is presented for analyzing and minimizing the effect of non-linearities associated with the optical power transfer function of a generic modulator, to inform choices of design and operation conditions. The Mach-Zehnder interferometer, micro-ring modulator, and ring-assisted Mach-Zehnder interferometer are compared using this method. The analysis is applied to compare three analog photonic processor architectures for machine learning applications, based on wavelength, space, and time division multiplexing. Our results indicate that despite the lower maximum resolution exhibited by Mach-Zehnder interferometers, they are the most balanced choice for space and time division multiplexing architectures due to stability and power consumption.

Although modern optical fiber communications typically rely on digital signals used to modulate an optical carrier, analog photonics has been the subject of focused research over the last decades. Original interest in analog photonic links stemmed from the low propagation loss offered by optical fibers in radio-over-fiber communications systems, providing an alternative to lossy coaxial cables[1], and has now arrived at enabling a scalable 5G fronthaul through antenna remoting[2]. Through the birth of the field of microwave photonics, applications expanded, taking advantage of the wide processing bandwidth offered by upconversion to optical frequencies[3]. In this way, many functionalities could be provided that were not viable in traditional RF systems. Notably, microwave photonic processors[4] could offer an advantage over digital electronics, as the energy consumption per task does not increase significantly as the bandwidth increases, and the use of integrated photonics in particular can drastically reduce size and power consumption. Photonics-enhanced radar is another unique application provided by microwave photonics[5], where the higher carrier frequencies and the broadened bandwidth offered by photonics result in smaller antennas and increased resolution compared to electronic radar transceivers.

In parallel, photonics for computing experienced an intermittent increase in research activity. Originally, logical gates based on light were investigated to overcome the constraints of the classic von Neumann computing architecture[6] and to solve the related interconnection issues in integrated electronics. However, the benefits of miniaturization of electronic components outweighed those offered by optical technologies. The main drawbacks of optical logic gates are their dimensions compared to digital electronic gates, and their limited ability to drive other cascaded gates, since the signals are represented with optical power that must be distributed to the output devices[7]. Nevertheless, recent breakthroughs in artificial intelligence have sparked attention in novel computational frameworks, reigniting interest in analog photonic computing. In general, optical neuromorphic devices are considered promising for any use case based on matrix-vector multiplication, including neural networks, scientific computing, and cryptography[8]. Focusing on the former, the surge in the use of neural networks over the last decade, with the associated large-scale energy consumption, prompted a consideration of alternative hardware.

In particular, integrated photonic technologies, implemented through photonic integrated circuits (PICs), offer unique advantages that synergize with both the fields of microwave and neuromorphic photonics. In the former, aside from reducing footprint and complexity compared to equivalent RF systems, they offer enhanced functionalities not available in bulk optics[3], for example, microwave generation with high spectral purity by means of Kerr micro-resonator combs[9]. In the latter, PICs enable unparalleled computing speeds per core[10], and novel computing paradigms, such as reservoir computing[11,12]. However, the benefits of using integrated photonic devices are hindered by the accumulation of noise and distortions in analog systems, which undermine their functionality and limit their scalability. All parts of analog systems contribute to the accumulation of noise and distortions, but the most critical components are fast light modulators, which are essential for the generation of optical signals. The optimization of the design of such modulators is instrumental in maximizing the potential of

[1]Scuola Superiore Sant'Anna, Via G. Moruzzi 1, Pisa, 56124, Italy. [2]Department of Information Engineering, University of Pisa, Via G. Caruso 16, Pisa, 56122, Italy. e-mail: lorenzo.demarinis@santannapisa.it

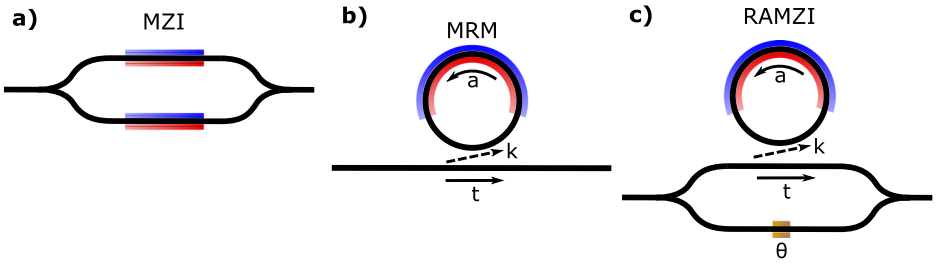

Fig. 1 | Schematic illustrating the three modulators analyzed. a Mach-Zehnder interferometer. **b** Micro-ring modulator. **c** Ring-assisted Mach-Zehnder interferometer. t and k indicate the coupling coefficients of the waveguide to the ring, a the single-pass transmission, and θ the DC phase shift introduced by the modulator arm without the ring.

photonic integration, since these key components ultimately set the limits of resolution, power consumption, footprint, bandwidth, and system complexity. This is true also in digital communication links, as discussed in ref. 13, where the design of different plasmonic modulators is directly related to the performance metrics of the link.

In this invited paper, we discuss the optimal design strategy of analog photonic modulators to counter noise and distortions. We focus on analog photonic processors for machine learning applications and the practical trade-off that must be considered in these systems. A complete neuromorphic processor is complex and requires careful co-design of the analog electronics for implementation of the non-linear activation function and data read-out, and consideration of the memory used to store neuron output[14]. Furthermore, the use of quantized training algorithms and inference is appropriate for analog photonic neural networks, where noise and distortions render floating point representation of data impracticable[15]. Further references to non-linearities in this paper refer to non-linear optical modulation and not the non-linearities required by neuromorphic computing architectures (for example in the activation function). Here we focus on the limitations introduced by the fast photonic modulators used in the matrix vector multiplication part of the processing. A theoretical method for analysing the linearity of a generic modulator is presented, illustrating how the linearity should be expected to depend on the selected bias point and on other modulator parameters. This method is applied to consider the design of three common modulators: the Mach-Zehnder Interferometer (MZI), the micro-ring modulator (MRM) and the ring-assisted Mach-Zehnder Interferometer (RAMZI). The implications of this analysis are then discussed at a system level by comparing several photonic neuromorphic architectures. The remainder of the paper is organized as follows: the Methods section introduces the three modulator architectures and their transfer functions and presents the method for analysis of the distortions induced by modulator non-linearities; the Results section applies the analysis to the three modulator architectures, and brings the discussion from the device level to the system level outlining the main trade-offs and issues arising when designing photonic processors; the Conclusions section summarizes the paper.

Methods

Modulator architectures

In this work, three modulator architectures commonly realized in integrated photonics were chosen for analysis. They are all based on an Electro-Optic (EO) phase modulation, which is then converted to an amplitude modulation. These are the Mach-Zehnder interferometer, the all-pass micro-ring modulator, and the ring-assisted Mach-Zehnder interferometer. The modulators are schematized in Fig. 1, where the blue and red elements represent the EO phase modulators, and the optical waveguides are represented in black.

The Mach-Zehnder interferometer (MZI), sketched in Fig. 1a, has been employed in optical communications for decades[16], and continues to set performance benchmarks[17–19] due to its stability and large bandwidth. It is simple to fabricate, consisting of two 3 dB couplers and phase modulation (PM) elements in one or both internal branches. Duplicated PM elements allow for relatively low driving power due to push-pull operation. The transfer function is the ratio of the modulator output and input powers; in the case of the MZI, its relatively simple form is given by:

$$T_{\mathrm{MZI}}(\phi) = \frac{1}{2}\left(1 - cos(\phi)\right), \tag{1}$$

where ϕ is the phase difference between the arms introduced by the PM elements. A purely sinusoidal transfer function is obtained as a function of ϕ, which does not result in a very linear behavior.

The all-pass micro-ring modulator (MRM), sketched in Fig. 1b, is also commonly found in the literature[20,21]. It consists of a straight waveguide directly coupled to a circular waveguide, where the PM element is distributed. MRMs generally have low footprint, insertion loss, and modulating power. However, a strong process control is required as the operating wavelength must be spectrally aligned with the edge of the transmission resonance, which is vulnerable to imperfections[22]; alternatively post-fabrication thermal trimming techniques can be employed, which allow spectral alignment of devices manufactured at the wafer scale, and thermal tuning to counteract real-time temperature oscillations[23]. The waveguide-ring coupler is characterized by the coupling coefficients: t (the self-coupling coefficient) and k (the cross-coupling coefficient); assuming a lossless coupler, $t^2 + k^2 = 1$.

Considering that the reflections back into the straight waveguide are negligible, the all-pass MRM transfer function is given by Bogaerts, W. et al. and Heebner, J. et al. [22,24]:

$$T_{\mathrm{MRM}}(\phi) = \frac{a^2 - 2tacos(\phi) + t^2}{1 - 2atcos(\phi) + (ta)^2}, \tag{2}$$

where ϕ is the single-pass phase shift, a is the single-pass transmission, given by the losses in the ring and coupler $a^2 = e^{-\alpha l}$, α is the power attenuation coefficient and l is the round-trip length. The previous assumption of $t^2 + k^2 = 1$ can introduce a small error in the magnitude of the transmitted power, but not in the width of the resonance, as long as the coupler losses are taken into account in α[22]. The values a and t for a fabricated ring are rarely reported, but can be derived from the values of finesse and extinction ratio[25], where the former can be extracted from the commonly reported Q-factor, free spectral range, and resonant wavelength[22].

The ring-assisted Mach-Zehnder interferometer (RAMZI), represented in Fig. 1c, consists of an MRM coupled to one of the internal branches of the MZI, where the branch without the MRM introduces a DC phase shift of θ. The main advantage it offers is to linearize the sinusoidal transfer function of the MZI, indeed impressive results in terms of linearity have been demonstrated in refs. 26,27. The transfer function is given by Tazawa and Steier[28]:

$$\begin{aligned} T_{\mathrm{RAMZI}}(\phi) &= \frac{1}{2}\left|\frac{1}{\sqrt{2}}a^*(\phi) + \frac{1}{\sqrt{2}}\mathrm{e}^{-i\theta}\right|^2, \\ A(\phi) &= \frac{t - a\mathrm{e}^{-i\phi}}{1 - at\mathrm{e}^{-i\phi}}, \end{aligned} \tag{3}$$

where relating to the ring: ϕ is the single-pass phase shift and $A(\phi)$ is the complex amplitude transfer function ($T_{\mathrm{MRM}}(\phi) = |A(\phi)|^2$).

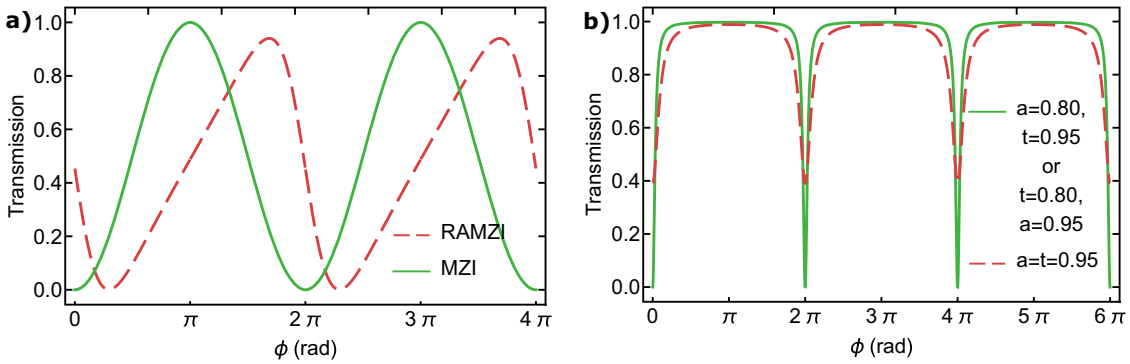

Fig. 2 | Transfer function of the analyzed modulators. In both figures, *a* represents the single-pass transmission and *t* the self-coupling coefficient of the ring, **a** MZI and RAMZI. **b** MRM for critical coupling, $a = t = 0.95$, and for over/under coupling $a = 0.95$, $t = 0.80$, or $a = 0.80$, $t = 0.95$.

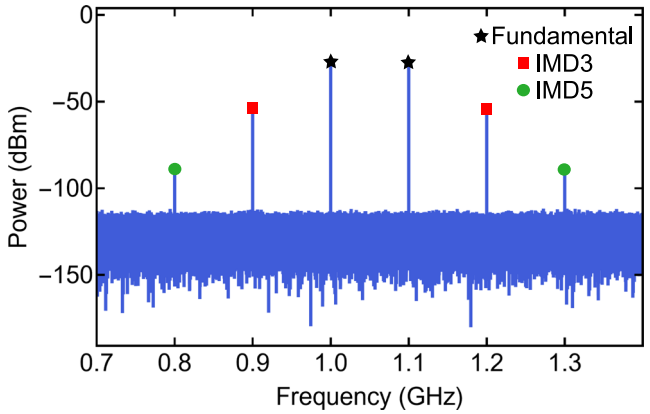

Fig. 3 | Example of the resulting two-tone test spectrum of the received photodiode signal around the fundamental frequencies, for a MZI with 10 dBm input power.

The transfer functions for the MZI and RAMZI are plotted in Fig. 2a. There are many free parameters in the RAMZI which affect the non-linearity characteristics of the transfer function[29]. The ring in the RAMZI is modeled with $a = 0.95$, the value of $t = 0.28$ is selected such that for $\theta = \pi/2$, the transfer function is linearized for small amplitude RF driving signals. One of the points for which this occurs is around $\phi \approx \pi$, which is evident in the figure. The losses introduced by the ring slightly reduce the extinction ratio with respect to the MZI.

The transfer function for the MRM is plotted in Fig. 2b for critical coupling, i.e., when the coupled power is equal to the power loss in the ring, for which $a = t = 0.95$ and for under (over) coupling ($a < t$ and $t < a$ respectively) for which the resonance peaks are the same: $a\,(t) = 0.80$, $t\,(a) = 0.95$. As the critical coupling condition is approached, the extinction ratio improves, the resonance peak becomes sharper, and for the same phase change induced by the PM, there is a larger effective change in the transmitted optical power.

Non-linearity analysis for analog photonic processor design optimization

Since non-linearities introduce distortions that limit the resolution of analog photonic processors, the analysis described in this, and the following section, is useful for choosing optimal parameters (e.g., bias point, splitting ratios) for the linear operation of modulators employed in analog processors for machine learning applications.

Generally, when an RF signal is applied to a modulator, the resulting signal will not solely contain components at the frequency of modulation due to the presence of non-linearities, caused inherently by the non-linear optical power transfer function of the modulator. The transfer function can be opportunely modified, leading to improved linearity, as in the case of the RAMZI. Non-linearities are also caused by the physical effect employed for phase modulation in some photonic integration technologies, i.e., the phase change induced by the modulator will not be linearly proportional to the applied bias, additionally there is a material and voltage-dependent attenuation (not accounted for by the static insertion loss), which affects the transfer function[30].

For modelling a device in a specific platform, the presence of these additional non-linear effects must be considered, and if appropriate, the optical power transfer function can be correspondingly modified[30]. In the case of $LiNbO_3$ devices, the phase modulation can be approximated as linear with applied voltage due to the exploitation of the Pockels effect, resulting from the non-centrosymmetry of the crystal, hence the analysis presented here will already be suitable without additional modification. For InP devices, which rely on the non-linear quantum-confined Stark effect, the induced change in phase was found to scale approximately with the applied electric field to the power of 1.57 over the C-band[31]. In the case of silicon photonics, the non-linear effect of carrier modulation can be simulated, as presented for an MRM in ref. 32. Each platform offers its own complications in terms of fabrication steps, commercial compatibility, and stability[33]. In this work, for the sake of generality and simplicity, only the non-linearities inherent in the transfer function are considered: we focus on the modulator dependent non-linearity characteristics to inform design and operation choices, rather than the material as in ref. 30.

In this context, the *two-tone test* is a commonly employed technique for analyzing the linearity of modulators. Considering a signal applied to a modulator:

$$V(t) = V_0 + A(cos(\omega_1 t) + cos(\omega_2 t)), \tag{4}$$

where V_0 is the bias voltage, A is the amplitude of the RF modulation and ω_1 and ω_2 two closely spaced, so-called fundamental, angular frequencies. The induced phase change, in the case of a linear EO effect, would be:

$$\phi(t) = \pi V(t)/V_\pi, \tag{5}$$

where V_π is the voltage required to induce a π change in phase. References to the phase modulation amplitude in the following text refer to the maximum value of this expression.

Due to non-linearities, various components will appear in the detected spectrum at different combinations of the angular frequencies ω_1 and ω_2, which are known as intermodulation distortions. The odd components of intermodulation distortions are of interest as they cannot be filtered since they fall close to the modulation frequency, and hence limit the resolution of an analog device; the two most significant are the third-order intermodulation distortion (IMD3) at angular frequencies $2\omega_1$-ω_2 and $2\omega_2$-ω_1, and fifth-order intermodulation distortion (IMD5) at angular frequencies $3\omega_1$-$2\omega_2$, $3\omega_2$-$2\omega_1$. The higher odd order IMDs generally have a lower impact as the distortion power reduces with the order. Figure 3 shows an

Table 1 | Amplitude coefficients at various frequency components for the two-tone test of a generic modulator, with power transfer function expanded up to the fifth order

Component	Frequency	Amplitude
Fundamental	ω_1, ω_2	$Aa_1 + \frac{9}{4}A^3a_3 + \frac{25}{4}A^5a_5$
IMD3	$2\omega_1$-ω_2, $2\omega_2$-ω_1	$\frac{3}{4}A^3a_3 + \frac{25}{8}A^5a_5$
IMD5	$3\omega_1$-$2\omega_2$, $3\omega_2$-$2\omega_1$	$\frac{5}{8}A^5a_5$

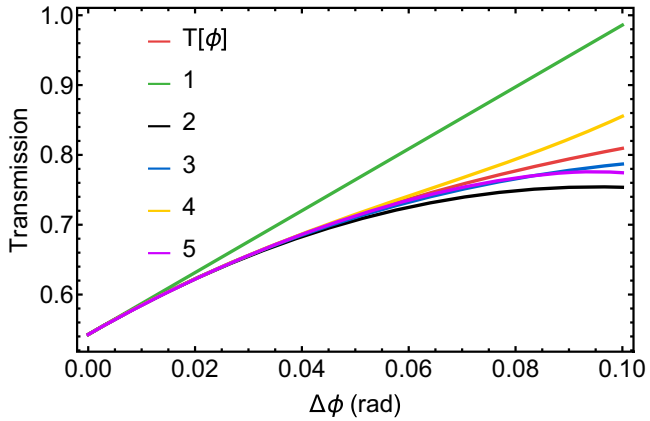

Fig. 4 | Transfer function of a ring ($a = t = 0.95$) expanded around the bias point for which the third-order intermodulation distortion is minimized at a phase amplitude of $\pi/100$. The numbers in the key indicate the order of expansion.

example of the resulting spectrum around the fundamental frequencies when the two-tone test is performed, in this case for an MZI biased at $\phi = \pi/2$ with RF input power per tone, $P_{in} = 10$ dBm, $\omega_1/2\pi = 1.0$ GHz and $\omega_2/2\pi = 1.1$ GHz; the fundamental, IMD3 and IMD5 components are highlighted. The relative power of the various frequency components can be assessed in order to understand where the bias point of the modulator should be selected for improved linear operation, and how this depends on other modulator parameters.

We start the non-linearity analysis by expanding the modulation device power transfer function as a function of a small change in phase (i.e., a small RF signal power) around the bias phase point $\phi_b = \pi V_0/V_\pi$, where V_0 is the applied bias voltage[1]:

$$T(\phi) = \sum_{k=0}^{\infty} a_k(\phi - \phi_b)^k, \tag{6}$$

where a_k are the expansion coefficients, defined as:

$$a_k = \frac{1}{k!}\left(\frac{d^k T}{d\phi^k}\right)_{\phi=\phi_b}. \tag{7}$$

Table 1 is obtained by substituting Equation (5) into (6), expanding up to the fifth order and collecting the terms at the frequencies of interest by performing a trigonometric reduction. It lists the amplitude of the various frequency components in the transfer function in terms of the expansion coefficients and amplitude of the modulating signal; as expected the amplitude of each component is dominated by the RF modulation amplitude elevated to the component order. For an MZI, since the optimal bias condition does not change with the amplitude of phase modulation, it is sufficient to consider terms up to the third order, as in ref. 1. On the other hand, for any modulators employing rings, expansion up to the fifth order is required to investigate large phase amplitude modulation, which is discussed in the following section.

If $T(\phi)$ is the optical power transfer function of a generic modulator, the power received at the photodiode is given by Marpaung[1]:

$$P_{diode} = \left(\frac{r_{PD}\,T(\phi)P}{L}\right)^2 \frac{R_L}{2}, \tag{8}$$

where r_{PD} is the responsivity of the photodiode, P is the optical power of the external laser, L is a factor accounting for optical losses, and R_L is the load resistance of the photodiode. The division by two is due to lossy impedance matching in receiver electronics, this assumes that a resistance matching that of the read-out electronics is placed in parallel with the photodiode, so half the power is delivered to this resistance and half to the read-out load.

Hence, given an optical power transfer function $T(\phi)$ of a modulator, we can analyse the device linearity by obtaining the powers in the received signal at the fundamental and non-linear distortion frequencies. In Fig. 4, the transfer function $T_{MRM}(\phi)$ of a critically coupled MRM ($a = t = 0.95$) is plotted together with the Taylor function approximation arising from different orders of expansion, to illustrate the range of suitability of the approximating function. $\Delta\phi$ is the difference in phase from the bias point, with the latter chosen such that the power in IMD3 is minimized for a phase amplitude of $\pi/100$. The numbers in the figure key indicate the order of expansion. Expanding up to the fifth order gives us an approximate function with less than 1% error compared to $T(\phi)$ for a range of $-0.05 \le \Delta\phi \le 0.07$, i.e. a range of 27% to 76% of the max value of $T(\phi)$.

Results

Modulator comparison

In the following we compare the three modulator architectures fed by an external continuous-wave (CW) laser. We focus on the relative power of fundamental and IMD components, with the aim of minimizing the impact of the latter in constraining the bit resolution of the analog photonic processor. In an analog photonic processor, the resolution of the driver electronics is also important, new commercial high-speed DACs can reach 16 bit resolution[34,35], with non-commercial DACs with lower power consumption reaching 8 bit resolution[36], hence the limiting factor here is considered to be the modulator. The typical parameters of a silicon photonics implementation, with a commercial external laser, are employed: 293 K temperature, 10 mW laser power, -150 Hz^{-1} laser relative intensity noise (RIN), 0.8 A/W photodiode responsivity, 3.5 dB grating coupler losses and 50 Ω photodiode load resistance. The MZI was assumed to have an EO phase modulator with $V_\pi = 5$ V and an insertion loss of 6 dB. The MRM is assumed to have a $V_\pi L = 0.6$ Vcm[37] with 80% of the circumference covered by the EO element, an insertion loss of 3 dB[20] and a ring radius of 15 μm, chosen as a compromise between driving voltage and footprint. For the RAMZI we assume a loss of 4 dB, similar to[38], $a = 0.95$, $t = 0.28$, and $\theta = \pi/2$, selected, as previously stated, to optimize linearity with a lossy ring; the insertion loss is generally lower than the MZI due to lower losses in the ring modulating element compared to a straight PM element. The ring of the RAMZI was again assumed to have $V_\pi L = 0.6$ Vcm with 80% EO element coverage assuming a similar fabrication process, but with a radius of 80 μm, the latter similar to[39]. A larger ring radius is required for the RAMZI to have a reasonable operating power since a larger phase modulation range is required compared to the MRM.

In Fig. 5, the relative power of the various frequency components is plotted both for the MZI and the RAMZI modulators for a phase modulation amplitude $\phi_a = \pi/2000$, corresponding to an RF input power $P_{in} = -33$ dBm for the RAMZI, and $P_{in} = -42$ dBm for the MZI. For the MZI, a choice of operating bias is obvious at $\phi_b = \pi/2$, as the IMD3 and IMD5 components follow the same trend as the fundamental power, and we have no choice but to maximise the power of all components together. There are no free parameters in the transfer function that can be adjusted to vary the non-linearity characteristics.

Contrastingly, both the RAMZI and MRM have multiple parameters in the transfer functions which alter the non-linearity characteristics. Furthermore, if a bias point is selected for which the power at the fundamental

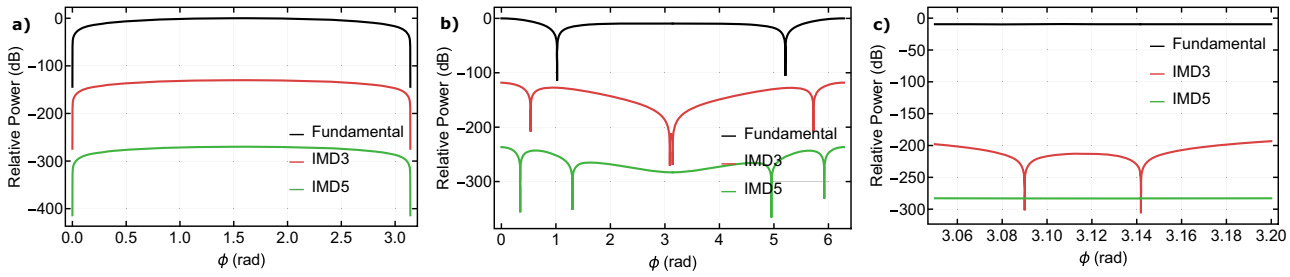

Fig. 5 | Intermodulation distorsion comparison. Relative power in the frequency components for the fundamental, third-order intermodulation distortion, IMD3, and fifth-order intermodulation distortion, IMD5, as a function of bias phase for a phase modulation amplitude = $\pi/2000$ (**a**) in the MZI, (**b**) in the RAMZI, (**c**) zoom around the IMD3 minima in (**b**).

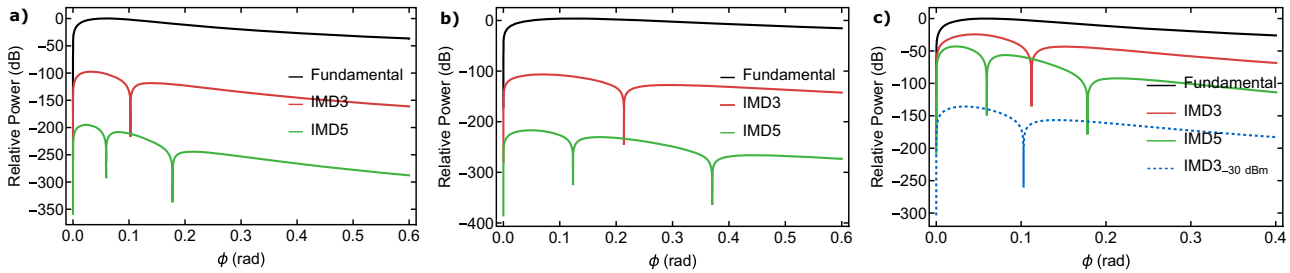

Fig. 6 | Relative power in the frequency components corresponding to the fundamental, third-order intermodulation distortion, IMD3, and fifth-order intermodulation distortion, IMD5, as a function of bias phase for the MRM. (**a**) $a = t = 0.95$, phase modulation amplitude = $\pi/8000$; (**b**) $a = 0.95$, $t = 0.80$, phase modulation amplitude = $\pi/8000$; (**c**) $a = t = 0.95$, phase modulation amplitude = $\pi/100$.

frequency is maximized, considerable power at the IMD3 and IMD5 frequencies would also be present, limiting the bit resolution of the analog photonic processor.

For the RAMZI, losses in the ring create an asymmetry in the transmission curve[29]. Using the analysis method presented here, the IMD3 power was minimized at RF input power $P_{in} = -33$ dBm, by optimizing the t and ϕ parameters, i.e., by finding the modulator parameters for best-case linear operation. This optimization results in double-peaked minima in the IMD3 curve: since both are close to the central point of the transmission curve (minima occurring around $\phi = \pi$), either may be chosen as a working point. Figure 5c shows an enlargement of this region, showing that IMD3 components are suppressed at the two minima.

In Fig. 6, the same analysis is performed for an all-pass MRM. In Fig. 6a and b, a small phase amplitude of $\pi/8000$ is considered (corresponding to a $P_{in} = -30$ dBm) for critically and non-critically coupled rings, respectively. We observe that IMD3 is minimized when the bias phase is set for 50% power transmission, which is why the minima shift rightwards for Fig. 6b, as the ring resonance peak is broadened (as shown in Fig. 2b). For a larger phase modulation amplitude of $\pi/100$, corresponding to $P_{in} = 8$ dBm, the bias phase at which IMD3 is minimized shifts higher, as shown in Fig. 6c, where the IMD3 for $P_{in} = -30$ dBm is plotted for comparison.

With the selection of the optimum bias point, the two-tone test is performed for the three modulator architectures and the relative powers, P_{out}, of the fundamental, IMD3 and IMD5 peaks are numerically obtained from the spectrum of the output signal as a function of P_{in}. The spurious free dynamic range (SFDR) can thus be analyzed, defined as the range of P_{in} for which the fundamental tone is above, but the IMD distortions are below or equal to the noise floor[40], which is usually the maximum signal to noise and distortion ratio (SINAD) achievable. From the SINAD, the effective number of bits can be obtained, defined as the number of bits used to digitally store the values that can be resolved by the analog system, which defines its resolution[41].

The power in the fundamental, IMD3, and IMD5 components is plotted as a function of the RF input power P_{in} in Figs. 7 and 8 at a set modulator bias phase. Figure 7a refers to the MZI, Fig. 7b to the RAMZI, and Fig. 8a and b to the critically coupled MRM with bias point optimized for small and large phase modulation amplitude, respectively. To find the SFDR, the noise floor must be calculated. The noise sources are assumed to be thermal, shot, and laser RIN. In logarithmic units, it is given by Marpaung[1]:

$$NF = 10\log_{10}\left(B\left((1+g)k_BT + \frac{qr_{PD}\overline{T(\phi)}PR_L}{2L} + 10^{\frac{RIN}{10}}\left(\frac{r_{PD}\overline{T(\phi)}P}{L}\right)^2\frac{R_L}{4}\right)\right), \quad (9)$$

where B is the bandwidth of the system, g is the link gain and modifies the thermal noise of the transmitter (usually negligible in absence of amplification, here assumed to be 0), k_B is the Boltzmann constant, T is the temperature, q is the electron charge, $\overline{T(\phi)}$ is the average value of the transmission function, and RIN is the relative intensity noise of the laser. The noise floor plotted in the figures corresponds to B = 1 Hz, which results in a SFDR unit of dBHz$^{\frac{n-1}{n}}$, where n represents the scaling order of the non-linearity.

Note that, apart from the MZI, the IMD3 and IMD5 do not necessarily scale with RF input power to the third and fifth order. From Fig. 7a, the SFDR limited by the third order non-linearity, SFDR3, is 103 dBHz$^{2/3}$, the IMD3 scales with P_{in}^3 and the IMD5 scales with P_{in}^5. The effects of linearizing the transfer function of the RAMZI are apparent in Fig. 7b, where both the IMD3 and the IMD5 scale with P_{in}^5. The bias point was chosen to minimize the IMD3 component at a phase modulation amplitude of $\pi/2000$ ($P_{in} = -33$ dBm). In this case the SFDR3 is 121 dBHz$^{4/5}$. If the bias point shifts, for example $\phi = 3.08$ rad instead of the $P_{in} = -33$ dBm minima at 3.09 rad (corresponding to an decrease of 0.3 %), the SFDR3 changes by less than 1 dBHz$^{4/5}$, demonstrating the robustness of the RAMZI to bias point fluctuation.

In Fig. 8a, the bias point ($\phi_b = 0.103$ rad) of the MRM was selected in order to minimize the IMD3 component at a phase modulation amplitude of $\pi/8000$, corresponding to $P_{in} = -30$ dBm. Again, as the RF power increases, IMD3 scales with P_{in}^5, the SFDR3 in this case is 119 dBHz$^{4/5}$. If the bias point is shifted lower by 0.3 %, the SFDR3 at 1 Hz bandwidth reduces by

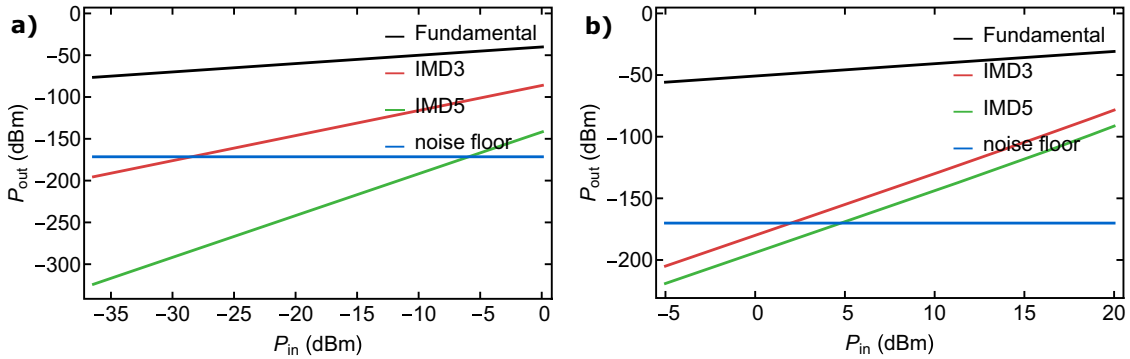

Fig. 7 | Fundamental and IMD power Vs input power for MZI and RAMZI. Relative power in the frequency components for the fundamental, third-order intermodulation distortion, IMD3, and fifth-order intermodulation distortion, IMD5, for a set phase as a function of the power of the RF driving signal for (**a**) MZI, $\phi_b = \pi/2$ (**b**) RAMZI, ϕ_b optimized for phase modulation amplitude = $\pi/2000$. Noise floor plotted for 1 Hz bandwidth.

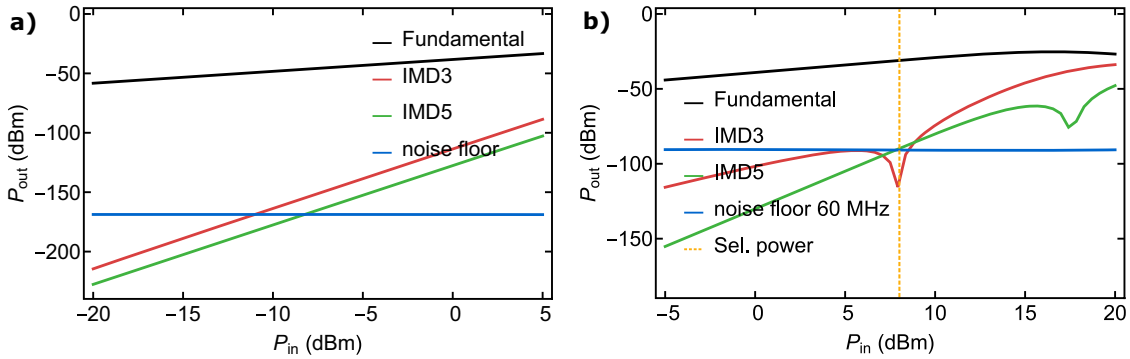

Fig. 8 | Fundamental and IMD power Vs input power for MRM. Relative power in the frequency components for the fundamental, third-order intermodulation distortion, IMD3, and fifth-order intermodulation distortion, IMD5, for a set phase as a function of the RF input power P_{in} for an MRM, $a = t = 0.95$ (**a**) ϕ_b optimized for phase modulation amplitude= $\pi/8000$, noise floor for 1 Hz bandwidth (**b**) ϕ_b optimized for phase modulation amplitude = $\pi/100$, noise floor for 60 MHz bandwidth.

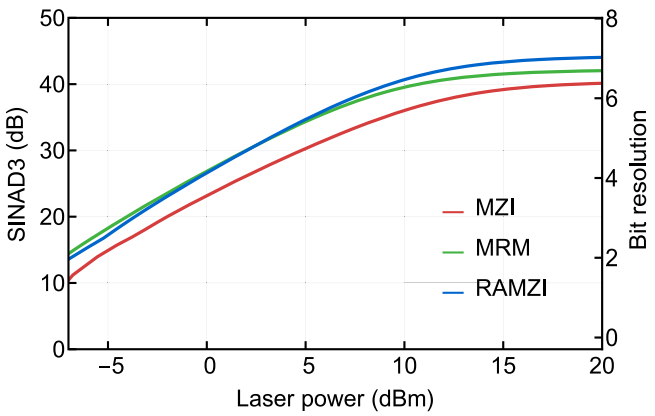

Fig. 9 | Comparison of signal to noise and distortion ratio limited by the third order distortion, SINAD3, and corresponding bit resolution for the three modulators as a function of external laser power, system bandwidth of 10 GHz.

3 dB, showing that, compared to the RAMZI, the MRM is sensitive to bias point phase drift. For a non-critically coupled ring with $a(t) = 0.95$, $t(a) = 0.80$ optimized with the same P_{in}, the SFDR3 reduces to 115 dBHz$^{4/5}$. In Fig. 8b, the bias point is selected to minimize the IMD3 component at a higher RF power of 8 dBm, ($\phi_b = 0.112$ rad, Fig. 6c), we observe that the IMD3 power dips below that of the IMD5 component at $P_{in} = 8$ dBm. This effect is present both for the RAMZI and MRM, even when the IMD3 is minimized for lower P_{in} (expected from Figs. 5c and 6a), but the minima are not visible within the range selected for plotting in Figs. 7b and 8a, as the power of the non-linearities are far under the 1 Hz noise floor when this phenomenon occurs.

To investigate whether an optimization of the MRM bias point for high P_{in} is worthwhile, we might consider a case where the noise floor is such that it coincides with the minima in IMD3 and thus the IMD5 component limits the SFDR. For $P_{in} = 8$ dBm and an external laser power of 10 dBm, this corresponds to a system bandwidth of around 60 MHz, resulting in a noise floor of −91 dBm, also represented in Fig. 8b. This results in a slight improvement in the SFDR compared to the case in which ϕ_b is selected to minimize the IMD3 component at lower P_{in}. The SFDR limited by the fifth order non-linearity is SFDR5=59.5 dB (corresponding to an effective bit resolution of 9.6), comparable with the low P_{in} optimization achieving an SFDR3 = 57.2 dB (corresponding to an effective bit resolution of 9.2). However, if the noise floor was lowered (by reducing the bandwidth of the system), the SFDR would worsen compared to the optimization for small P_{in}.

Note that a similar effect is achievable with the RAMZI modulator, however in this case the optimization of the bias phase of the ring modulator is not sufficient, and the parameter t must also be optimized as it was previously for P_{in}= -33 dBm. In practice, this may be changed dynamically with a thermally-tuned coupler[42].

In Fig. 9, the maximum value of the signal to noise and distortion ratio limited by the third order distortion, namely SINAD3, is reported as a function of the external laser power for the three modulators at 10 GHz bandwidth. Here the high-power non-linear two-photon and free-carrier absorption effects are not considered, which would be present in silicon and InP platforms. The nomenclature of SINAD, rather than SFDR, was chosen due to the levelling-off of the fundamental curve at the P_{in} operating point required for a 10 GHz noise floor. The bias phase of the RAMZI and MRM

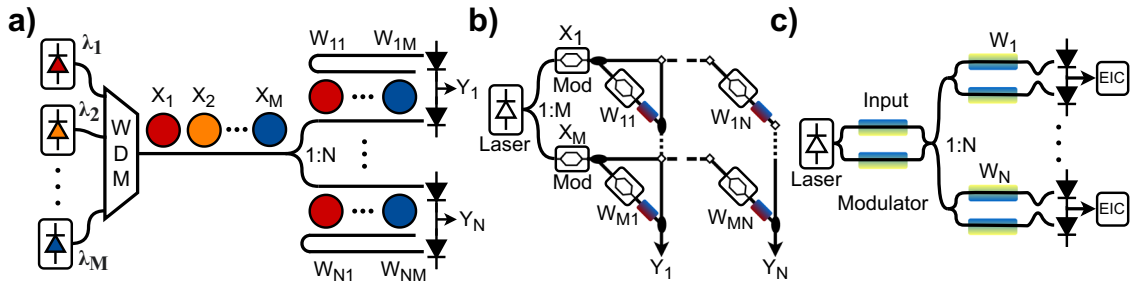

Fig. 10 | Considered photonic neural network architectures. a Micro-ring weight bank, (**b**) Coherent photonic crossbar, (**c**) Photonic electronic multiply-accumulate neuron.

are set to minimize the IMD3 component for small P_{in}. The laser power modifies the power in the fundamental, IMD3, and IMD5 components, as well as the level of noise floor. The effective bit resolution is displayed on the right axis. We observe the best performance from the RAMZI as the power is increased, with a maximum bit resolution of around 7. The curves levels off as the upper limit to the SINAD, set by the RIN of the laser, is approached[41]. The MZI exhibits the worst performance, with a maximum bit resolution of 6.3; additionally, compared to the MRM/RAMZI, the performance considerably worsens when the optical power is lowered. If the bandwidth were to be lowered, the difference in performance between the MRM/RAMZI and MZI would become more pronounced, as the IMD3 components for the MRM/RAMZI scale with P_{in}^5 and for a smaller bandwidth the noise floor is lower, requiring a lower P_{in} to reach an optimum signal to noise and distortion ratio.

For the critically-coupled MRM, by choosing to optimize the bias point at higher P_{in} in accordance with the 10 GHz noise floor (similar to Fig. 8b), a marginal improvement in the bit resolution of 0.1 is found; the effect of optimization is smaller compared to lower noise floor/bandwidth due to the fundamental power levelling off at high P_{in}. For the non-critically coupled ring with a, $(t) = 0.95$, t, $(a) = 0.8$, the upper limit of the SINAD3 at 10 GHz reduces to 36 dB with an equivalent bit resolution of 5.7.

Case study on analog photonic processors for machine learning applications

The previous section presented the design strategies and the operating point optimization needed to maximise the effective bit resolution of different optical modulators. In this section, we move from the device level to the system level and report a practical methodology for addressing the issues and trade-offs that arise when designing analog photonic processors. In our numerical analysis, we consider three system architectures, which resemble the three main multiplexing strategies used to implement feedforward photonic neural networks: wavelength division multiplexing (WDM), coherent PICs with spatial division multiplexing (SDM), and time division multiplexing (TDM)[43].

Figure 10a shows the micro-ring weight bank[44], an architecture that relies on multiple wavelengths to encode inputs. As the modulator must be wavelength-selective, the only choice is to use MRM both for input encoding and for weighting. In this solution, M lightwaves coming from different lasers are multiplexed within a single waveguide and modulated by M micro-rings to impress the inputs. The resulting amplitude-modulated WDM vector is broadcast to N weighting units, each composed of M add-drop MRMs that impress both positive and negative weights by unbalancing the light power in each wavelength between its upper and lower waveguides. Finally, the WDM signals are collected by N balanced photodetectors whose photocurrents create the output vector.

As this device requires a modulator to encode each input and weight, its complexity scales quadratically with the number of inputs and outputs $O(M \cdot N)$, and thus the required footprint and electrical connections. Moreover, the higher the number of outputs, the lower the optical power transmitted to each weighting unit. Usually, the input MRMs are fast and the weighting ones are slow, i.e., the former are based on electro-optic modulators and the latter rely on thermal tuning. As in every photonic device, the design of the fast modulators is critical, as they set the limits of speed, resolution, and power consumption of the whole system[41]. Usually, the power consumption is the most critical aspect, so the aim here could be to use a low driving power such that no RF amplifiers are needed. Considering a 4-input device, a peak-to-peak voltage, V_{pp}, of 0.5 V, a laser power of 10 mW, a ring finesse of 16, an extinction ratio of 16 dB, an insertion loss of 0.9 dB, $V_\pi L$ of 0.6 Vcm, 12 μm radius[37], and with 80 % of the circumference covered by the EO element, an effective bit resolution at the input of 3.3 bits is achieved at 10 GHz. The optimal bit resolution of 6.4 is achieved with a higher V_{pp} of 4.1 V. Once the resolution of the input stage is fixed, the thermal MRMs in the weighting banks can be designed accordingly, a lower quality factor can be tolerated, thus avoiding trimming techniques[23]. Nevertheless, precise feedback control loops are required to counteract thermal drifts and other interference effects as micro-rings suffer from stability issues[45].

The coherent photonic crossbar array[46], depicted in Fig. 10b, is a recently-proposed interferometric structure able to realise both real- and complex-valued matrix operations. Differently from coherent unitary processors[47], it allows for a direct mapping of inputs and weights, and is able to attain a great fidelity (> 99.9%) even with structures scaled towards high number of inputs and weights[48]. The device performs vector-matrix multiplications through the coherent recombination of modulated light via nested modulators within a splitting and recombining tree configuration made of M rows and N columns, resembling M inputs and N outputs. Thermal shifters are added to the diagonal branches to support complex value operations. To balance the power within the vertical branches, the splitting ratio of the successive 1×2 branches are adjusted accordingly.

Being a coherent processor, a good control over phase is required, and thus the use of MZIs or RAMZIs avoids the need for complex feedback loops that would be required to adjust the highly non-linear phase/voltage relation of rings. Still, MRMs could be used if the system design were to target a reduced footprint. Because of the direct mapping of inputs and weights, this system requires a modulator to encode each parameter, so the number of modulators scales as $O(M \cdot N)$. The choice of MZIs reduces the footprint compared to RAMZIs. Again, the input modulators are usually fast, thus being the most critical devices. As discussed in the previous sub-section, for any RF power the optimal MZI bias point is fixed at the 3-dB point. Accounting for a laser power of 10 dBm, 6 dB losses due to the power splitting, and 6 dB insertion loss of the MZI, a 4-input architecture can achieve 4.5 effective bits at 10 GHz, with a V_{pp} of 1.6 V for a V_π of 5 V. To increase the resolution, RAMZIs can be used at the input instead of the MZIs. In this case, assuming a $V_\pi L$ of 0.6 Vcm, a ring with a radius of 80 μm with an EO element length of 80% of the circumference and an insertion loss of 4 dB, a bit resolution of 5.2 is achieved for a signal with a V_{pp} of 9.1 V. Such a high driving voltage may, however, be impractical due to the increased power consumption, cost, and size of the driving electronics. For this reason the peak-to-peak voltage could be reduced down to 0.5 V at a cost to the bit resolution, which would be reduced to 2.4 and 2.9 bits for the MRM and MZI respectively.

Table 2 | Comparison between the photonic neural network architectures with different modulators

Architecture	MRM Resolution Driving voltage	MZI Resolution Driving voltage	RAMZI Resolution Driving voltage
Micro-ring	3.3–6.4 bits	-	-
Weight Bank	0.5–4.1 V		
Coherent	2.4–5.6 bits	2.9–4.5 bits	1.1–5.2 bits
Photonic Crossbar	0.5–4.8 V	0.5–1.6 V	0.5–9.1 V
PEMAN	3.3–6.4 bits	4.6–5.7 bits	2.6–6.5 bits
	0.5–4.1 V	0.5–1.1 V	0.5–7.5 V

The resolution is given as a range between that corresponding to a driving peak-to-peak voltage of 0.5 V, and the maximum achievable one. All computations target 4-branches devices with a 10 GHz modulation.

The last architecture considered is the photonic-electronic multiply-accumulate neuron (PEMAN)[14], whose scheme is outlined in Fig. 10c. This TDM architecture performs fast multiplications in the photonic domain, while the accumulation part is performed within a custom analog electronic front-end. In a single time frame, the first modulator impresses an input in the amplitude of a lightwave, which is in turn broadcast to N weighting units, implementing N different neurons. Each weight unit is composed of a 1×2 modulator and a balanced photodetector, whose output photocurrent encodes the result of the dot-product multiplication between input and weights $X_i \cdot W_j$. The N branches parallelize the computations of N neurons, where the weights per neuron are time-multiplexed. The number of supported connections (weights) per neuron can be as high as some hundreds[14], and depends on the analog electronic frontend.

Differently from the other two architectures, a key advantage of the PEMAN is that the number of modulators is constant with respect to the number of inputs and outputs: the complexity scales with $O(N)$ and with four branches, only five modulators are needed in total. Nevertheless, the system design is more complex as every modulator is high-speed and a co-design with the custom analog electronic frontend is required. This architecture can use any kind of modulator, with the choice depending on specific design priorities: for instance, in ref. 43 electro-absorption modulators were used to realize the photonic part of the PEMAN. The main performance metrics that undergo a trade-off are: footprint, speed, power consumption, resolution, optical losses, and complexity of the driving electronics. Relying on MRMs would provide the lowest footprint, a reduced power consumption, and a good bit resolution, but post-fabrication trimming techniques and/or stabilization feedback are required, with the latter increasing the energy consumption. The MZIs do not guarantee the highest resolution, have a large footprint, but also good stability, large bandwidth, and would require a simpler bias circuitry. A RAMZI based device would provide the highest resolution, at the price of all other metrics. Considering a laser power of 10 dBm and the above-reported losses for each modulator type, at 10 GHz and the maximum driving voltage the PEMAN could achieve 6.4, 5.7 and 6.5 bits of input resolution, for an MRM, MZI, or RAMZI, respectively. Here, we are approximating the resolution to that of the input modulator, which results the same as the whole circuit as detailed in the related publications[14,41].

Table 2 reports a direct numerical comparison of the three systems with different composite modulators, in terms of the achievable resolution reported at different driving voltages, showing how modulator choice affects the processor performance. The resolution is given in a range, targeting a 4-branch device, a modulation frequency of 10 GHz, and the above-reported parameters for modulators and architectures. The minimum resolution quoted for each modulator is calculated at a driving peak-to-peak voltage of 0.5 V, while the maximum V_{pp} gives the best resolution achievable. We report the driving voltage as a key metric as it is directly related to the complexity of the elctronic circuitry and its power consumption. In particular, using a $V_{pp} < 1$ V would allow for direct driving of CMOS circuitry, avoiding bulky, expensive, and energy intensive RF drivers. Still, the reported resolution results must be considered as the upper limit achievable by photonic modulators, the driving and reading electronic circuitry inevitably introduce additional quantization noise and distortions[49]. For all the considered cases, the minimum resolution is above 2 equivalent bits, except when using the RAMZI in the coherent crossbar as the RAMZI requires a higher driving power, and in a coherent architecture a single laser is split between several branches with a corresponding power penalty. Conversely, at the price of a high driving voltage, the RAMZI assures the highest resolution. The power consumption is a lot higher than the MRM, as the latter can be driven with a voltage equal to a small proportion of the V_π to achieve large output intensity modulation, while the ring loaded on the RAMZI requires a larger fraction of V_π to achieve the same dynamic. The driving voltage can be reduced by increasing the ring radius, with a negative impact on the footprint. In all cases, increasing the laser power would increase the resolution up to the limit imposed by its RIN[41], though this may not be feasible in practice due to non-linear absorption effects at high power.

From this comparison the MZI is demonstrated to be the most suitable modulator for the PEMAN and the coherent crossbar, providing a good trade-off between resolution and driving voltages. Notably, our analysis revealed that microrings can provide a high resolution with relatively low driving voltages. However, unless the footprint is paramount in the analog system, the MRM is the most suitable modulator for the photonic weight bank only, due to the need of precise fabrication/post-fabrication trimming and a precise locking of the bias point. The RAMZI provides a resolution advantage compared to the MZI, but requires a much higher driving voltage. In the case of the photonic crossbar, where lower optical power reaches the modulators, the RAMZI performance drops below that of the microring modulator. Hence, it should be considered only for TDM architectures when maximum optical resolution is required.

Conclusions

Analog photonics has the potential to bring significant benefits in a wide variety of applications, including brain-inspired computing architectures and programmable microwave photonic processors. The recent advancements in fabrication processes allow for higher yields and more degrees of freedom in the design of photonic components, enhancing the potential of these systems. In this paper, we presented a method for analysing the linearity of a generic optical modulator, and applied it to three common modulators, namely the MRM, the MZI and the RAMZI, in order to inform design and operational decisions for optimising SFDR and effective bit resolution. We then reported the issues to be tackled and the trade-offs when using such modulators in a whole system, considering practical examples of three common neural network photonic processors. The chosen architectures exemplify the three main multiplexing strategies used in neuromorphic PICs: the micro-ring weight bank for WDM; the coherent crossbar for SDM; and the photonic-electronic neuron for TDM. We discussed the impact of the modulator choice, its design, and the required driving voltage, representative of electronic circuit complexity and power consumption. Microring modulators allow for the implementation of WDM architectures, and offer good resolution even at low driving voltages. However, they require a precise fabrication/post-fabrication trimming and require stabilization during operation. Mach-Zehnder modulators strike a better balance between stability, resolution and required voltage, and should be regarded as the primary choice for SDM and TDM architectures, unless a reduced footprint is paramount, for which MRMs are preferable. The ring-assisted MZIs achieve the highest resolution; despite being more robust to bias point fluctuation than MRMs, the difference in achievable resolution is small and they require almost double the driving voltage. Furthermore, in reduced optical power scenarios, as in the coherent crossbar architecture, the RAMZI maximum resolution drops below that of the MRM, making it less practical.

Data availability

Data available on request from the authors.

Code availability

The code used for analysis is available upon request from the authors.

Received: 22 October 2024; Accepted: 17 March 2025;
Published online: 26 March 2025

References

1. Marpaung, D. A. I. *High dynamic range analog photonic links: design and implementation*. Doctoral thesis, University of Twente (2009).
2. Rommel, S. et al. Towards a Scaleable 5G Fronthaul: Analog Radio-over-Fiber and Space Division Multiplexing. *J. Lightwave Technol.* **38**, 5412–5422 (2020).
3. Marpaung, D., Yao, J. & Capmany, J. Integrated microwave photonics. *Nat. Photonics* **13**, 80–90 (2019).
4. Pérez, D., Gasulla, I. & Capmany, J. Toward Programmable Microwave Photonics Processors. *J. Lightwave Technol.* **36**, 519–532 (2018).
5. Ghelfi, P. et al. A fully photonics-based coherent radar system. *Nature* **507**, 341–345 (2014).
6. Sawchuk, A. & Strand, T. Digital optical computing. *Proc. IEEE* **72**, 758–779 (1984).
7. Jiao, S. et al. All-optical logic gate computing for high-speed parallel information processing. *Opto-Electron. Sci.* **1**, 220010 (2022).
8. McMahon, P. L. The physics of optical computing. *Nat. Rev. Phys.* **5**, 717–734 (2023).
9. Liang, W. et al. High spectral purity Kerr frequency comb radio frequency photonic oscillator. *Nat. Commun.* **6**, 7957 (2015).
10. Totović, A. R., Dabos, G., Passalis, N., Tefas, A. & Pleros, N. Femtojoule per MAC neuromorphic photonics: an energy and technology roadmap. *IEEE J. Sel. Top. Quantum Electron.* **26**, 1–15 (2020).
11. Shen, Y.-W. et al. Deep photonic reservoir computing recurrent network. *Optica* **10**, 1745–1751 (2023).
12. Picco, E., Lupo, A. & Massar, S. Deep photonic reservoir computer for speech recognition. *IEEE Transactions on Neural Networks and Learning Systems* (2024).
13. Blatter, T. et al. Ring-assisted, racetrack, and Mach-Zehnder modulator: which one offers the lowest voltages and chirp-free operation? *Opt. Express* **32**, 37968–37983 (2024).
14. De Marinis, L. et al. A codesigned integrated photonic electronic neuron. *IEEE Journal of Quantum Electronics* **58** (2022).
15. Paolini, E. et al. Photonic-aware neural networks. *Neural Comput. Appl.* **34**, 15589–15601 (2022).
16. Kawanishi, T. *Integrated Mach–Zehnder Interferometer-Based Modulators for Advanced Modulation Formats* (pp. 273–286. Springer Berlin Heidelberg, Berlin, Heidelberg, 2010).
17. Alam, M. S. et al. Net 220 Gbps/λ IM/DD Transmssion in O-Band and C-Band With Silicon Photonic Traveling-Wave MZM. *J. Lightwave Technol.* **39**, 4270–4278 (2021).
18. Ahmed, A. N. R. et al. High-efficiency lithium niobate modulator for K band operation. *APL Photonics* **5**, 091302 (2020).
19. Ogiso, Y. et al. 80-GHz Bandwidth and 1.5-V V_{π} InP-Based IQ Modulator. *J. Lightwave Technol.* **38**, 249–255 (2020).
20. Zhang, Y. et al. 240 gb/s optical transmission based on an ultrafast silicon microring modulator. *Photon. Res.* **10**, 1127–1133 (2022).
21. Alexander, K. et al. Nanophotonic Pockels modulators on a silicon nitride platform. *Nat. Commun.* **9**, 3444 (2018).
22. Bogaerts, W. et al. Silicon microring resonators. *Laser Photonics Rev.* **6**, 47–73 (2012).
23. Jayatilleka, H. et al. Post-fabrication trimming of silicon photonic ring resonators at wafer-scale. *J. Lightwave Technol.* **39**, 5083–5088 (2021).
24. Heebner, J., Grover, R. & Ibrahim, T. *Optical Microresonators: Theory, Fabrication, and Applications*. (Springer, Springer-Verlag New York 2008, 2008).
25. McKinnon, W. R. et al. Extracting coupling and loss coefficients from a ring resonator. *Opt. Express* **17**, 18971–18982 (2009).
26. Feng, H. et al. Ultra-high-linearity integrated lithium niobate electro-optic modulators. *Photon. Res.* **10**, 2366–2373 (2022).
27. Zhang, C., Morton, P. A., Khurgin, J. B., Peters, J. D. & Bowers, J. E. Ultralinear heterogeneously integrated ring-assisted Mach-Zehnder interferometer modulator on silicon. *Optica* **3**, 1483–1488 (2016).
28. Tazawa, H. & Steier, W. Bandwidth of linearized ring resonator assisted Mach-Zehnder modulator. *IEEE Photonics Technol. Lett.* **17**, 1851–1853 (2005).
29. Yang, J. et al. Influence of loss on linearity of microring-assisted Mach-Zehnder modulator. *Opt. Express* **12**, 4178–4188 (2004).
30. Jacques, M. et al. Modulator material impact on chirp, DSP, and performance in coherent digital links: comparison of the lithium niobate, indium phosphide, and silicon platforms. *Opt. Express* **26**, 22471–22490 (2018).
31. Klein, H. *Integrated InP Mach-Zehnder Modulators for 100 Gbit/s Ethernet Applications using QPSK Modulation*. Doctoral thesis, Berlin: Technische Universität (2010).
32. Ayazi, A., Baehr-Jones, T., Liu, Y., Lim, A. E.-J. & Hochberg, M. Linearity of silicon ring modulators for analog optical links. *Opt. Express* **20**, 13115–13122 (2012).
33. Sinatkas, G., Christopoulos, T., Tsilipakos, O. & Kriezis, E. E. Electro-optic modulation in integrated photonics. *J. Appl. Phys.* **130**, 010901 (2021).
34. Texas Instruments. *DAC38RFxx Dual-Channel, Single-Ended, 14-Bit, 6- and 9-GSPS, RF-Sampling DAC With JESD204B Interface and On-Chip GSM PLL Data Sheet* (2017).
35. Analog Devices. *Dual, 16-Bit, 12.6 GSPS RF DAC with Wideband Channelizers Data Sheet* (2018).
36. Menolfi, C. et al. A 112gb/s 2.6pj/b 8-tap ffe pam-4 sst tx in 14nm cmos. In IEEE (ed.) *2018 IEEE International Solid-State Circuits Conference - (ISSCC)*, 104–106 (2018).
37. Yuan, Y. et al. A 5 × 200 Gbps microring modulator silicon chip empowered by two-segment Z-shape junctions. *Nat. Commun.* **15**, 918 (2024).
38. Gutierrez, A. M. et al. Ring-assisted mach–zehnder interferometer silicon modulator for enhanced performance. *J. Lightwave Technol.* **30**, 9–14 (2012).
39. Shawon, M. J., Wang, R. & Saxena, V. Design and modeling of silicon photonic ring-based linearized rf-to-optical modulator. In IEEE (ed.) *2018 IEEE 61st International Midwest Symposium on Circuits and Systems (MWSCAS)*, 348–351 (2018).
40. Urick Jr, V. J., McKinney, J. D. & Williams, K. J. *Fundamentals of Microwave Photonics*. (Wiley, Hoboken, New Jersey, United States, 2015).
41. De Marinis, L., Andriolli, N. & Contestabile, G. Analysis of integration technologies for high-speed analog neuromorphic photonics. *IEEE J. Select. Top. Quant. Electron.* **29**, 1–19 (2023).
42. Liu, Y. et al. Tunable and reconfigurable microwave photonic bandpass filter based on cascaded silicon microring resonators. *J. Lightwave Technol.* **40**, 4655–4662 (2022).
43. Roumpos, I. et al. Silicon integrated photonic-electronic neuron for noise-resilient deep learning. *Opt. Express* **32**, 34264–34274 (2024).
44. Tait, A. N. et al. Neuromorphic photonic networks using silicon photonic weight banks. *Sci. Rep.* **7**, 7430 (2017).
45. Tait, A. N. et al. Feedback control for microring weight banks. *Opt. express* **26**, 26422–26443 (2018).
46. Giamougiannis, G. et al. A coherent photonic crossbar for scalable universal linear optics. *J. Lightwave Technol.* **41**, 2425–2442 (2023).
47. De Marinis, L. et al. Photonic Integrated Reconfigurable Linear Processors as Neural Network Accelerators. *Appl. Sci.* **11**, 6232 (2021).
48. Moralis-Pegios, M., Giamougiannis, G., Tsakyridis, A., Lazovsky, D. & Pleros, N. Perfect linear optics using silicon photonics. *Nat. Commun.* **15**, 5468 (2024).

49. Tsakyridis, A. et al. Photonic neural networks and optics-informed deep learning fundamentals. *APL Photonics* **9**, 011102 (2024).

Acknowledgements
We acknowledge financial support under the National Recovery and Resilience Plan (NRRP), Mission 4, Component 2, Investment 1.1, Call for tender No. 1409 published on 14.9.2022 by the Italian MUR, funded by the European Union - NextGenerationEU - Project PRIN 2022 PNRR "LINUS". This work was also partially supported by the Italian Ministry of Foreign Affairs and International Cooperation, grant number PGR02045, and the Italian Ministry of Education and Research (MUR) in the framework of the FoReLab project (Departments of Excellence).

Author contributions
The analytical method and numerical analysis was implemented by P.S.K., supervision by L.D.M.; theoretical model assessment N.A., L.D.M.; neuromorphic systems analysis P.S.K., L.D.M.; writing—original draft preparation, P.S.K., L.D.M., N.A., funding acquisition, G.C.; all authors contributed to the writing and review of the manuscript.

Competing interests
The authors declare no competing interests.

Additional information
Supplementary information The online version contains supplementary material available at https://doi.org/10.1038/s44172-025-00395-5.

Correspondence and requests for materials should be addressed to Lorenzo De Marinis.

Peer review information *Communications Engineering* thanks the anonymous reviewers for their contribution to the peer review of this work. Primary Handling Editors: [Chaoran Huang] and [Anastasiia Vasylchenkova]. Peer review reports are available.